Self-Resonant Coil With High-Order Compensation Characteristics

Zixuan Yi, *Member, IEEE*, Qingfei Zhang, *Student Member, IEEE*, Shuang Li, *Student Member, IEEE*,
Xue-Xia Yang, *Senior Member, IEEE*, Dan Zeng, *Senior Member, IEEE*, and Meiling Li, *Member, IEEE*

***Abstract*—Self-resonant (SR) coils replace lumped with distributed compensation components, enabling efficient power transfer and high integration. However, current SR coils function merely as series (S) or parallel (P) resonant tanks, thereby supporting merely four low-order compensation networks: SS, SP, PS, and PP. High-order compensation networks have demonstrated superiority over low-order counterparts, providing enhanced safety, stability, and design flexibility. Unfortunately, no SR coil currently with high-order compensation network characteristics. This article proposes a novel SR coil with LCC compensation characteristics that integrates the required compensation components in the form of distributed structures with the main coil on a single substrate, eliminating lumped components. To verify feasibility, a pair of SR coils, incorporating a normal SR coil, are fabricated, which constitute a SR coil inductive power transfer (IPT) system with LCC-S compensation characteristics. Different with traditional LCC-S systems, the compensation inductor in the proposed SR coil participates in power transfer. Therefore, corresponding formulas for the resonant frequency, ac–ac power transfer efficiency (PTE), output voltages and power are provided. Favorably, the proposed IPT system exhibits three advantages: a constant voltage output independent of the ac load, high ac–ac PTE over a wide range of ac load values, independence of resonant frequency from coupling coefficients, and no damage to the front-end power source during no-load operation. Experimental results demonstrate a coil-to-coil PTE of 93.2% and dc–dc efficiency of 80.5% over a 35 mm spacing gap. In addition, a LED monitor is successfully powered, indicating its potential for application in electronic devices, such as mobile phones and laptops.**

***Index Terms*—Compensation networks, inductive power transfer (IPT), LCC-S, self-resonant (SR) coils.**

I. Introduction

INDUCTIVE power transfer (IPT) represents a prominent trend in the advancement of wireless power transmission (WPT) [1], [2], [3], [4]. In contrast to capacitive power transfer, microwave power transfer, and other WPT technologies, IPT provides superior biological safety [5], thereby attracting considerable research interest. This method utilizes ac power to energize the primary coil, generating a varying magnetic field. An electromotive force can be induced on the secondary coil, which is placed into the magnetic field. However, the presence of leakage inductance can lead to the generation of reactive power in the system, thus reducing transmission efficiency. To address this issue, it is typically necessary to employ compensation networks [6], [7] to tune the coupling structure so as to realize resonance at the operating frequency, which means achieving zero phase angle between the voltage and current.

For traditional IPT systems, the components required for compensation networks usually exist in the form of external lumped components. During system operation, significant electric field intensity or current density can be generated within the limited space of the external lumped capacitors. This situation may result in capacitors breakdown or change their nominal value, thus causing system detuning [8], [9], [10]. Moreover, as the operating frequency increases, the Q of the capacitors decreases, which leads to a high loss, thereby reducing the transmission efficiency, where Q is the quality factor. Self-resonant (SR) coils replace the external lumped capacitors with the distributed capacitors, enhancing the system stability and transmission efficiency, and effectively solving the aforementioned issues [11], [12], [13], [14], [15], [16], [17], [18], [19], [20], [21]. Current research on SR coils primarily focuses on coupling enhancement, Q improvement, and compensation networks. Coupling enhancement can be achieved through shielding techniques [11] and [13]. A novel circuit modeling approach, the extended IEM, was proposed for SR coils with ferrite shielding [11], and a comprehensive shielding technique for SR coils was introduced in [13]. The use of nanocrystalline materials [14], [15] also enhances coupling, offering superior performance compared to conventional magnetic materials. To improve the Q of SR coils, structural design of the coils is employed to reduce conduction losses [16], [17], [18], [19], [20], where multilayer thin copper foil structures [16], [17] mitigate losses by sharing current across layers. Yi et al. [12] optimized the ratio of winding width

Received 12 September 2024; revised 7 February 2025 and 2 April 2025; accepted 2 May 2025. Date of publication 8 May 2025; date of current version 30 June 2025. This work was supported by the National Natural Science Foundation of China under Grant 52207214 and Grant 62171270. Recommended for publication by Associate Editor K. Park. *(Corresponding author: Meiling Li.)*

Zixuan Yi, Qingfei Zhang, Xue-Xia Yang, Dan Zeng, and Meiling Li are with the School of Communication and Information Engineering, Key laboratory of Specialty Fiber Optics and Optical Access Networks, Joint International Research Laboratory of Specialty Fiber Optics and Advanced Communication, Shanghai Institute for Advanced Communication and Data Science, Shanghai University, Shanghai 200444, China (e-mail: yizixuan@shu.edu.cn; zqf@shu.edu.cn; yang.xx@shu.edu.cn; dzeng@shu.edu.cn; meilingli@shu.edu.cn).

Shuang Li is with the University of Michigan-Shanghai Jiao Tong University Joint Institute, Shanghai Jiao Tong University, Shanghai 200240, China (e-mail: lishuang77@sjtu.edu.cn).

Color versions of one or more figures in this article are available at https://doi.org/10.1109/TPEL.2025.3568066.

Digital Object Identifier 10.1109/TPEL.2025.3568066

to the spacing between adjacent windings to reduce loss. The gradual-width SR coil in [18] increases trace width in high-current regions, reducing total loss. A modified segmented filament model for helical SR coils was proposed [19], along with a high-efficiency self-resonant unequal-pitch coil design. From the perspective of compensation networks, there are currently two types of SR coils: 1) series-type and 2) parallel-type, which can form IPT systems of four low-order compensation networks (SS, SP, PS, and PP) [6], [7]. SS compensation network boasts a simple structure and a resonant frequency that is independent of the coupling coefficient, however, the primary current is inversely proportional to the coupling coefficient. Hence, when the primary and secondary coils are far apart or under no-load conditions, the primary current can be rapidly increased, causing power supply damage and compromising the safety of the system [22], [23]. The resonant frequencies of the other three low-order compensation networks are related to the coupling coefficient, resulting in poor stability [24]. Compared to low-1order compensation networks, high-order compensation networks such as LCL–LCL [25], LCC-S [26], [27], [28], and LCC–LCC [29], [30], [31] can simultaneously satisfy high safety standards, independence of the resonant frequency from the coupling coefficient, and offer lower load sensitivity as well as higher design flexibility. In summary, SR coils enhance the efficiency, integration, and stability of IPT systems. However, the current SR coils can only form IPT systems based on four low-order compensation networks, which limits their development and application potential.

In order to retain the advantages of SR coils while overcoming their limitations, this article introduces, for the first time, a SR coil with high-order compensation network characteristics that integrates the required compensation components in the form of distributed structures with the main coil on a single dielectric substrate, eliminating the need for any lumped components. SR coils with high-order compensation network characteristics combine the advantages of high-order compensation networks and SR coils, enhancing system stability, safety, and efficiency. Moreover, they maintain high transmission efficiency while increasing coil integration and have great potential for application in electronic devices such as mobile phones, LED monitors, and laptops.

This article proposes the SR coil with LCC compensation characteristics (LCC SR coil) for the first time. To verify its feasibility, a novel SR coil IPT system with LCC-S compensation characteristics is constructed, and its advantages and characteristics are analyzed through equivalent circuit analysis and verified through experiments. The rest of this article is organized as follows. In Section II, the novel SR coil with LCC compensation characteristics is proposed, followed by a physical model correlating the physical dimensions of the LCC SR coil with its electrical characteristics. In Section III, a SR coil IPT system with LCC-S compensation characteristics is constructed to verify the feasibility. Different with the traditional LCC-S systems, the compensation inductor integrated on the proposed coil also participates in power coupling. the proposed LCC-S SR coil IPT system is analyzed through the equivalent circuit method. In Section IV, an optimized dimension design of coils for the LCC-S SR coil IPT system coil operating at 13.56 MHz is proposed, and the ondition for the independence of resonant frequency from coupling coefficients. In Section V, the transmission characteristics of the proposed IPT system, including a constant voltage output that is independent of the ac load, high-efficiency transmission(87%–93.2%) across a wide range of ac load(10 Ω–50 Ω) variations are validated through ac–ac experiments. Additionally, a dc–dc experiment was conducted using a power analyzer, achieving a dc–dc efficiency of 80.5%. A demonstration of wirelessly powering a display screen at a distance of 35 millimeters is also presented. Finally, Section VI concludes this article.

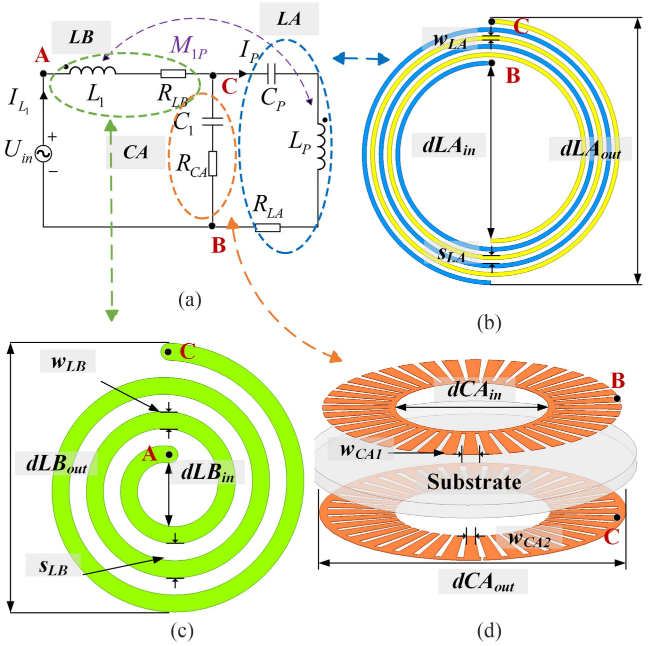

(a) (b) (c) (d)

Fig. 1. (a) Equivalent circuit of LCC SR coil. (b) Main coil *LA*. (c) Compensation coil *LB*. (d) Parallel capacitor *CA*.

II. SR COIL WITH LCC COMPENSATION CHARACTERISTICS

In this section, the detailed structure of the SR coil with LCC compensation characteristics is proposed, followed by a physical model correlating the physical dimensions of the LCC SR coil with its electrical characteristics.

A. *Structure of SR Coil With LCC Compensation Characteristics*

To ensure that the LCC SR coil has the same characteristics as a normal coil compensated by the traditional LCC network, the equivalent circuit of the former, as shown in Fig. 1(a), should be consistent with that of the latter. This article divides the equivalent circuit of the LCC SR coil into three parts, which are the main coil *LA*, the compensation coil *LB*, and the parallel capacitor *CA* and are identified by blue, green, and orange oval dashed border, as shown in Fig. 1(a). The connection points between these three parts are identified as A, B, and C, respectively, where, Point A is located at one end of the series inductor L_1 and

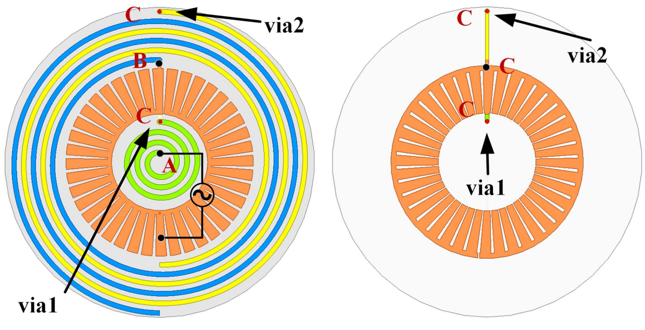

(a) (b)

Fig. 2. LCC SR coil structure. (a) Top view. (b) Bottom view.

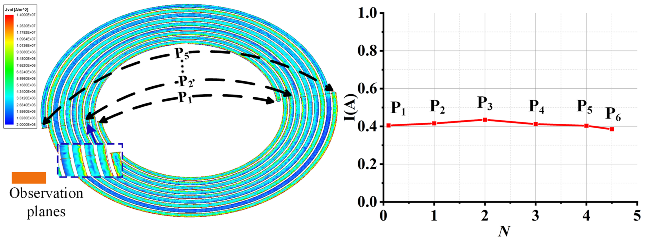

(a) (b)

Fig. 3. (a) Current distribution of the two windings of LA under the excitation of 1 W. (b) Total current in both windings of each turn.

is connected to one of the poles of the power supply. Point B is connected to one plate of the parallel capacitor C_1, to one end of the main inductor L_P, and to another pole of the power supply. Point C is connected to the other end of the series inductor L_1, the other plate of the parallel capacitor C_1, and another end of the main inductor L_P. The implementation approach for the LCC SR coil is to design the above three parts as distributed structures, and then integrate them onto one dielectric substrate. First, since the series SR coil can be equivalently considered as a series connection of an inductor and a capacitor, the main coil is designed as a planar bifilar coil [31], [32], as shown by the blue and yellow metal windings in Fig. 1(b), corresponding to the main inductor L_P and series capacitor C_P in Fig. 1(a). In Fig. 1(b), Point B and Point C are two ends of the main coil *LA*, respectively. Next, the compensation coil *LB*, as indicated by the green metal winding in Fig. 1(c), corresponds to the series inductor L_1 in Fig. 1(a), which is designed as a structure in the form of a planar spiral coil. Finally, the parallel capacitor *CA* is designed as two symmetrically distributed gear-shaped metal plates on the upper and lower surfaces of the dielectric substrate, as indicated by the two orange metal conductors in Fig. 1(d), which corresponds to the parallel compensation capacitor C_1 in Fig. 1(a), where, the inner width of each tooth w_{CA1} of the gear is smaller than the outer width w_{CA2}. As shown in Fig. 1(d), Point B and Point C are located on the upper and lower plates of the parallel capacitor, respectively. Point A and Point C are located at the two ends of the compensation coil, respectively.

The overall coil structure of the LCC SR coil is shown in Fig. 2, where Fig. 2(a) and (b) is the top and bottom views of the LCC SR coil, respectively. On the substrate, from the inside to the outside are the compensation coil *LB*, the parallel capacitor *CA*, and the main coil *LA*, respectively. The yellow, blue, orange, and green parts representing metal conductors, while the white circular plate representing the dielectric substrate. The main coil *LA*, the compensation coil *LB* and one plate of the parallel capacitor *CA* are located on the front side of the substrate, as shown in Fig. 2(a), while the other plate of the parallel capacitor is located on the back side of the substrate, as shown in Fig. 2(b). According to the Points A, B, and C in the three parts shown in Fig. 1, route the traces on the substrate, connecting points marked with the same letters using the shortest possible traces to minimize unnecessary parasitic effects as much as possible. Point A and any point on the upper plate of the parallel capacitor are connected to an ac source. Since the compensation coil and the main coil are placed on the same dielectric substrate, extra mutual inductance M_{1P} between *LA* and *LB* is generated compared to the traditional LCC compensation network, as shown in Fig. 1(a), which may affect the resonant frequency, so it is necessary to further analyze the performance of the IPT system employing LCC SR coil to verify the feasibility of it.

B. Physical Model That Correlates the Physical Dimensions of the LCC SR Coil With Its Electrical Characteristics

The inductance of planar open SR coils [32] can roughly equal to traditional planar circular spiral coils with the same parameters. In contrast to the SR coils in [32], the two windings of *LA* are symmetrically arranged about the center. To verify the characteristics, the total current in both windings of each turn was recalculated using the method in [32]. The current distribution of the two windings is shown in Fig. 3(a), where a pair of transverse observation planes is added along the diameter for each turn. The initial pair of observation planes is denoted as P_1. Given that N_{LA} (the turn numbers of *LA*) = 4.5, a total of six pairs of observation planes are considered. The total current for each pair is shown in Fig. 3(b). The results confirm that the total current in both windings of each turn is equal. As *LA* can be equivalently considered as a series connection of the main inductor L_P and the series capacitor C_P. Therefore, the inductance of L_P is approximately equivalent to that of a conventional planar circular spiral coil with the same dimensions as *LA*, which can be calculated by [15]

$$L_P = \frac{\mu {N_{LA}}^2 d_{avg}}{2}\left(\ln\frac{2.46}{\rho} + 0.2\rho^2\right) \tag{1}$$

where $d_{avg} = ((\mathrm{d}LA_{\mathrm{in}} + \mathrm{d}LA_{\mathrm{out}})/2)$, $\rho = ((\mathrm{d}LA_{\mathrm{out}} - \mathrm{d}LA_{\mathrm{in}})/(\mathrm{d}LA_{\mathrm{out}} + \mathrm{d}LA_{\mathrm{in}}))$, respectively. Additionally, μ is the magnetic permeability and N_{LA} is the turn number of the coil. As *LB* is a conventional planar circular spiral coil, corresponding to the series inductor L_1. L_1 can also can be calculated by (1).

The electric field distribution between the two windings of *LA* is shown in Fig. 4, where electric walls appear between the windings. C_P can be derived as follows [33]:

$$C_P = (l_1 + l_n)\frac{C_E C_I}{C_E + C_I} + \sum_{k=2}^{n-1} l_k \frac{C_I}{2} \tag{2}$$

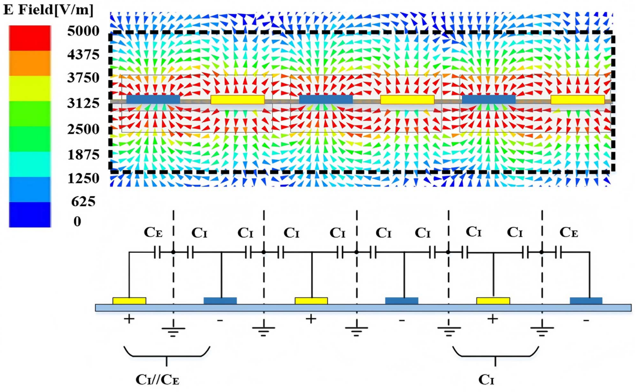

Fig. 4. Cross-sectional electric field distribution along *LA* radius.

where

$$C_I = 2C_{I,\text{air}} + C_{I,s} = \varepsilon_0 \left[2\frac{K(k_{I\infty})}{K(k'_{I\infty})} + (\varepsilon_\text{s} - 1)\frac{K(k_{I,s})}{K(k'_{I,s})} \right]$$

$$C_\text{E} = 2C_{\text{E,air}} + C_{\text{E,s}} = \varepsilon_0 \left[2\frac{K(k'_{\text{E}\infty})}{K(k'_{\text{E}\infty})} + (\varepsilon_\text{s} - 1)\frac{K(k'_{\text{E,s}})}{K(k'_{\text{E,s}})} \right].$$

The values of C_I and C_E are the sum of capacitances under different cases. The subscripts air and *s* indicate that the capacitance comes from the air and the substrate, respectively. ε_s is the relative permittivity of the substrate. *K*(*k*) is the complete elliptic integral of the first kind with modulus *k*. *k*' is the complementary modulus, where $k' = (1\text{-}k^2)^{1/2}$. Moreover, l_k ($k = 1, 2, \ldots, n$) represent the length of the metal winding for each turn, *n* represents the total number of turns in both windings, with $n = 2N_{LA}$.

As the parallel capacitor *CA* is designed as two symmetrically distributed gear-shaped metal plates on the upper and lower surfaces of the dielectric substrate, C_1 can be calculated by [34]

$$C_1 = \frac{\varepsilon_\text{s} S}{4\pi k d} \tag{3}$$

where ε_s is the relative permittivity of the substrate, *k* is the electrostatic constant, *d* is the distance between the two plates, and *S* is the area of the plates facing each other.

M_{1P} is the mutual inductance between the main inductor L_P and the series inductor L_1, which, from the coil model perspective, represents the mutual inductance between *LA* and *LB*. Since the inductance of L_P is approximately equivalent to that of a conventional planar circular spiral coil with the same dimensions as *LA*, the mutual inductance can be calculated using the filament method [35], [36], [37]. The cross-sections of *LA* and *LB* are divided into $(2M_0{+}1) \times (2N_0{+}1)$ and $(2m_0{+}1) \times (2n_0{+}1)$ small cells, as shown in Fig. 5. Each cell in each coil contains one filament, and the current density in the coil cross section is assumed to be uniform. With this assumption, the mutual inductance of the two circular coils is computed as the average sum of the total mutual inductances of each pair of filamentary coils [36]

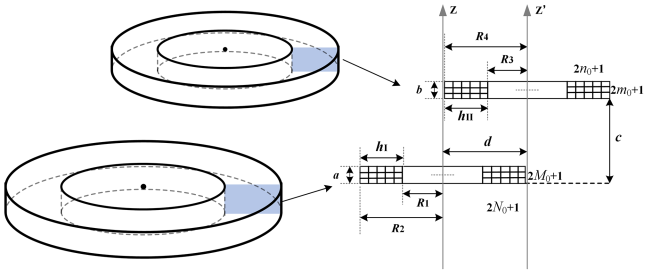

Fig. 5. Cross-sections of the two coils.

$$M_{1P} = \frac{N_1 N_2 \sum_{g=-M_0}^{g=M_0} \sum_{h=-N_0}^{h=N_0} \sum_{s=-m_0}^{s=m_0} \sum_{l=-n_0}^{l=n_0} M_{12}(g,h,s,l)}{(2M_0{+}1)(2N_0{+}1)(2m_0{+}1)(2n_0{+}1)} \tag{4}$$

where

$$\begin{aligned}
M_{12} = {} & \frac{\mu_0 \sqrt{R_{11}(h) R_{22}(l)}}{k(g,h,s,l)} \times \\
& \left\{ \left[2 - k^2(g,h,s,l) \right] \cdot K\left[k(g,h,s,l) \right] \right. \\
& \left. -2E\left[k(g,h,s,l) \right] \right\} \\
k^2(g,h,s,l) &= \frac{4R_{11}(h) R_{22}(l)}{\left[R_{11}(h) + R_{22}(l) \right]^2 + z^2(g,s)} \\
R_{11}(h) &= R_\text{I} + \frac{h_\text{I}}{2N_0 + 1} h h = -N_0, \ldots, 0, \ldots, N_0 \\
R_{22}(l) &= R_\text{II} + \frac{h_\text{II}}{2n_0 + 1} l l = -n_0, \ldots, 0, \ldots, n_0 \\
R_\text{I} &= \frac{R_1 + R_2}{2}, R_\text{II} = \frac{R_3 + R_4}{2} \\
R_1 &= \frac{dLA_\text{in}}{2}, R_2 = \frac{dLA_\text{out}}{2}, \\
R_2 &= \frac{dLB_\text{in}}{2}, R_2 = \frac{dLB_\text{out}}{2} \\
h_\text{I} &= R_2 - R_1, h_\text{II} = R_4 - R_3 \\
z(g,s) &= d + \frac{a}{(2M_0 + 1)} g + \frac{b}{(2m_0 + 1)} s \\
& g = -M_0, \ldots, 0, \ldots, M_0, s = -m_0, \ldots, 0, \ldots, m_0.
\end{aligned}$$

The other mutual inductances can also be calculated using (4).

III. ANALYSIS OF THE SR COIL IPT SYSTEM WITH LCC-S COMPENSATION CHARACTERISTICS

To verify the feasibility of the proposed LCC SR coil, a SR coil IPT system with LCC-S compensation characteristics is proposed in this section. A traditional LCC-S compensated IPT system uses lumped components and places the compensation

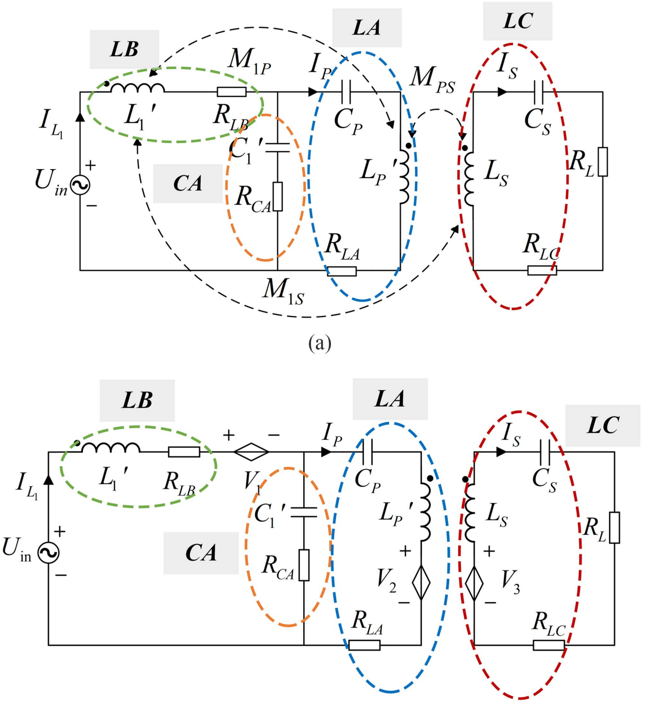

(a)

(b)

Fig. 6. (a) AC Equivalent circuit of SR coil IPT system with LCC-S compensation characteristics. (b) AC Equivalent circuit of SR coil IPT system with LCC-S compensation characteristics after decoupling M_{1P}.

inductor far from the main coils, making the coupling coefficients related to the compensation inductor (extra coupling coefficients) can be neglected negligible. In contrast, the LCC SR coil designed in this article integrates the required compensation components in the form of distributed parameter with the main coil on a single dielectric substrate, where the extra coupling coefficients cannot be ignored. Therefore, a detailed analysis of this SR coil IPT system with LCC-S compensation characteristics is required. By means of the equivalent circuit, the proposed IPT system is analyzed, and a new formula for the resonant frequency, efficiency, output voltage and power is derived.

The equivalent circuit of the SR coil IPT system with LCC-S compensation characteristics constructed by the LCC SR coil and a series SR coil is depicted in Fig. 6(a). The primary LCC SR coil comprises main coil *LA*, corresponding to the main inductor L_P and series capacitor C_P, compensation coil *LB*, corresponding to the series inductor L_1, and the parallel capacitor *CA*, corresponding to the parallel compensation capacitor C_1. The secondary series SR coil *LC*, similarly to the LCC SR main coil *LA*, is also structured as a planar open-bifilar coil, which corresponds to the main inductor L_S and series capacitor C_S in Fig. 7(a), as shown in Fig. 7(b), therefore, L_S and C_S can be calculated by (1) and (2). M_{PS} is the mutual inductance between the main inductors L_P and L_S, M_{1P} and M_{1S} are the extra mutual inductances between L_1 and L_P, and between L_1 and L_S. R_{LA}, R_{LB}, R_{CA}, and R_{LC} are the loss of *LA*, *LB*, *CA*, and *LC*, respectively.

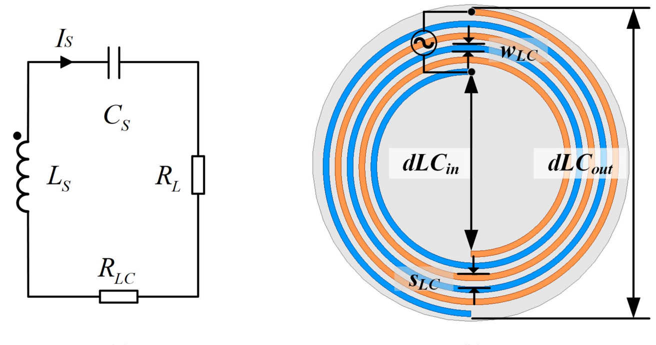

(a) (b)

Fig. 7. (a) Equivalent circuit of series SR coil. (b) Series SR coil LC.

For ease of analysis, the coupled primary inductors L_1 and L_P can be decoupled by inducing mutual inductance M_{1P} and the circuit is transformed into an equivalent circuit containing equivalent inductors L_1' and L_P', equivalent capacitor C_1' and controlled voltage sources, as shown in Fig. 6(b). The relevant parameters can be expressed

$$\begin{cases} L_1' = L_1 + M_{1P} \\ L_P' = L_P + M_{1P} \\ C_1' = \frac{1}{\frac{1}{C_1} + \omega^2 M_{1P}} \end{cases}, \begin{cases} V_1 = -j\omega M_{1S} I_S \\ V_2 = -j\omega M_{PS} I_S \\ V_3 = j\omega M_{PS} I_P + j\omega M_{1S} I_{L_1} \end{cases}. \tag{5}$$

The KVL equations can be obtained as follows:

$$\begin{cases} U_{\text{in}} + j\omega M_{1S} I_S = (j\omega L_1' + R_{LB}) I_{L_1} + \left(\frac{1}{j\omega C_1'}\right. \\ \quad \left. + R_{CA}\right)(I_{L_1} - I_P) \\ \left(\frac{1}{j\omega C_1'} + R_{CA}\right)(I_{L_1} - I_P) = \left(\frac{1}{j\omega C_P'} + j\omega L_P' + R_{LA}\right) I_P \\ \quad - j\omega M_{PS} I_S \\ j\omega M_{PS} I_P + j\omega M_{1S} I_{L_1} = \left(\frac{1}{j\omega C_2} + j\omega L_S + R_L + R_{LC}\right) I_S. \end{cases} \tag{6}$$

When the primary coil and secondary coil satisfy the resonance conditions

$$j\omega_0 L_P + \frac{1}{j\omega_0 C_1} + \frac{1}{j\omega_0 C_P} = 0 \tag{7}$$

$$\frac{1}{j\omega_0 C_2} + j\omega_0 L_S = 0. \tag{8}$$

The output current I_S and the current of primary inductor I_P can be expressed as

$$I_S = \frac{j\omega M_{PS} I_P + j\omega M_{1S} I_{L_1}}{R_L + R_{LC}} \tag{9}$$

$$I_P = \frac{\frac{1}{j\omega_0 C_1'} + R_{CA} - \frac{{\omega_0}^2 M_{PS} M_{1S}}{R_L + R_{LC}}}{Z_A} I_{L_1} \tag{10}$$

where Z_A can be defined as

$$Z_A = \frac{{\omega_0}^2 {M_{PS}}^2}{R_L + R_{LC}} + R_{LA} + R_{CA}. \tag{11}$$

Substituting (9) and (10) into (6), the relationship between the input voltage U_{in} and the input current I_{L1} can be obtained, therefore the input impedance Z_{in} can be expressed as in (12), shown at the bottom of this page.

According to (12), the imaginary part of the input impedance can be expressed as

$$\operatorname{Im}\left[Z_{\text{in}}\right]=\omega_0 L_1{}'-\frac{1}{\omega_0 C_1{}'}-\frac{2\omega_0 M_{PS}M_{1S}}{Z_A C_1{}'\left(R_L+R_{LC}\right)}+\frac{2R_{CA}}{Z_A\omega_0 C_1{}'}. \tag{13}$$

The main coupling coefficient K_{PS} between the coils is typically set between 0.1 to 0.3, and Z_A is directly proportional to K_{PS}, therefore

$$\begin{cases} R_{LA}+R_{CA} \ll \frac{\omega_0{}^2 M_{PS}{}^2}{R_L+R_{LC}} \\ \frac{2R_{CA}}{Z_A\omega_0 C_1{}'} \ll \omega_0 L_1{}' - \frac{1}{\omega_0 C_1{}'} - \frac{2\omega_0 M_{PS}M_{1S}}{Z_A C_1{}'(R_L+R_{LC})}. \end{cases} \tag{14}$$

The influence of R_{LA} and R_{CA} on Im[Z_{in}] can be neglected. Thus, (13) can be simplified as

$$\operatorname{Im}\left[Z_{\text{in}}\right]=\omega_0 L_1{}'-\frac{1}{\omega_0 C_1{}'}\left(1+2\frac{M_{1S}}{M_{PS}}\right). \tag{15}$$

Therefore, the resonant frequency can be expressed as

$$\omega_0=\sqrt{\frac{1}{C_1}\left(\frac{1+2\frac{K_{1S}}{K_{PS}}\sqrt{\frac{L_1}{L_P}}}{L_1\left(1-2\frac{K_{1S}}{K_{PS}}K_{1P}\right)}\right)}. \tag{16}$$

According to (12), the real part of the input impedance can be expressed as

$$\text{Re}[Z_{\text{in}}]=R_{LB}+R_{CA}+\frac{1}{C_1{}'^2\omega_0{}^2 Z_A}-\frac{R_{CA}{}^2}{Z_A}+a+b \tag{17}$$

where,

$$a=\frac{\omega_0{}^2 M_{1S}{}^2\left(R_{CA}+R_{LA}\right)}{\left(R_{LA}+R_{CA}\right)\left(R_L+R_{LC}\right)+\omega_0{}^2 M_{PS}{}^2} \tag{18}$$

$$b=\frac{2\omega_0{}^2 M_{1S}M_{PS}R_{CA}}{\omega_0{}^2 M_{PS}{}^2+\left(R_L+R_{LC}\right)\left(R_{LA}+R_{CA}\right)}. \tag{19}$$

Since $R_{CA}{}^2<<Z_A$, $R_{CA}{}^2/Z_A$ can be neglected in Re[Z_{in}]. Additionally, the compensation inductor L_1 is smaller than the primary main inductor L_P, and the main mutual inductance M_{PS} is much larger than the cross-coupling mutual inductance M_{1S}, thus

$$\omega_0{}^2 M_{PS}{}^2 \gg \omega_0{}^2 M_{1S}{}^2\left(R_{CA}+R_{LA}\right) \tag{20}$$

$$\omega_0{}^2 M_{PS}{}^2 \gg 2\omega_0{}^2 M_{1S}M_{PS}R_{CA}. \tag{21}$$

So that a and b can be neglected in Re[Z_{in}]. Therefore, (17) can be simplified as

$$\text{Re}[Z_{\text{in}}]=R_{LB}+R_{CA}+\frac{1}{C_1{}'^2\omega_0{}^2 Z_A}. \tag{22}$$

According to (22), the primary current I_{L1} at resonant frequency can be expressed as

$$I_{L_1}=\frac{U_{\text{in}}}{\text{Re}[Z_{\text{in}}]}=\frac{U_{\text{in}}}{R_{CA}+R_{LB}+\frac{1}{C_1{}'^2\omega_0{}^2 Z_A}}. \tag{23}$$

Since Z_A is an expression concerning $M_{PS}{}^2$, the primary current I_{L1} is inversely proportional to the mutual inductance $M_{PS}{}^2$. As the transmission distance increases, I_{L1} decreases. When unloaded, Z_A drops to its minimum, equal to the sum of the two losses R_{LB} and R_{CA}. At this point, Re[Z_{in}] is at its maximum, resulting in the minimum I_{L1}, thereby causing no damage to the front-end power source during no-load operation.

Substituting (23) into (9) and (10), the secondary current I_S can be expressed as

$$\begin{aligned} I_S &= \frac{U_{\text{in}}M_{PS}}{C_1{}'Z_A\text{Re}\left[Z_{\text{in}}\right]\left(R_L+R_{LC}\right)}\left(1+j\beta\right) \\ &= \frac{U_{\text{in}}M_{PS}}{C_1{}'Z_A\text{Re}\left[Z_{\text{in}}\right]\left(R_L+R_{LC}\right)}\sqrt{1+\beta^2}\angle\varphi \end{aligned} \tag{24}$$

where

$$\beta=\omega_0 C_1{}'\left[R_{CA}+\left(R_{LA}+R_{CA}\right)\frac{M_{1S}}{M_{PS}}\right] \tag{25}$$

$$\varphi=\arctan\beta. \tag{26}$$

Since

$$\begin{cases} \omega_0 C_1{}' \ll 1 \\ R_{CA}+\left(R_{LA}+R_{CA}\right)\frac{M_{1S}}{M_{PS}}<1 \end{cases}. \tag{27}$$

Therefore, $\varphi\approx 0$. The imaginary part of the secondary current I_S can be neglected. Equation (24) can be simplified as

$$I_S=\frac{U_{\text{in}}M_{PS}}{C_1{}'Z_A\text{Re}[Z_{\text{in}}]\left(R_L+R_{LC}\right)}. \tag{28}$$

The output voltage U_O can be expressed as

$$U_o=I_S R_L=\frac{U_{\text{in}}M_{PS}R_L}{C_1{}'Z_A\text{Re}\left[Z_{\text{in}}\right]\left(R_L+R_{LC}\right)}. \tag{29}$$

When $R_L>>R_{LC}$, (29) can be approximated as

$$U_O\approx UinC_1{}'M_{PS}\omega_0{}^2. \tag{30}$$

$$\begin{aligned} Z_{\text{in}} = {} & j\omega_0 L_1{}'+R_{LB}+\frac{1}{j\omega_0 C_1{}'}+R_{CA}-\left(\frac{1}{j\omega_0 C_1{}'}+R_{CA}\right)\frac{\frac{1}{j\omega_0 C_1{}'}+R_{CA}-\frac{\omega_0{}^2 M_{PS}M_{1S}}{R_L+R_{LC}}}{Z_A} \\ & +\frac{\left[\omega_0{}^2 M_{1S}{}^2+\omega_0{}^2 M_{1S}M_{PS}\left(\frac{\frac{1}{j\omega_0 C_1{}'}+R_{CA}-\frac{\omega_0{}^2 M_{PS}M_{1S}}{R_L+R_{LC}}}{Z_A}\right)\right]}{R_L+R_{LC}}. \end{aligned} \tag{12}$$

TABLE I
EQUIVALENT CIRCUIT PARAMETERS OF LCC-S SR COIL IPT SYSTEM

Parameter	Value
Primary main inductor L_P	4.451 μH
Primary series inductor L_1	1.04 μH
Primary parallel capacitor C_1	111.8 pF
Primary series capacitor C_P	42.3 pF
Secondary main inductor L_S	2.515 μH
Secondary series capacitor C_2	54.775 pF
Main coupling coefficient K_{PS}	0.16
coupling coefficient K_{1P}	-0.093
K_{1S}/K_{PS}	-0.205

Therefore, at resonant frequency, the SR coil IPT system with LCC-S compensation characteristics approximates a constant voltage output that is independent of the load.

The output power and transmission efficiency of the coils can be expressed as

$$P_{\text{out}} = R_L \left(\frac{U_{\text{in}} M_{PS}}{C_1{}' Z_A \text{Re}\left[Z_{\text{in}}\right] \left(R_L + R_{LC}\right)} \right)^2 \tag{31}$$

$$\eta = \frac{R_L {M_{PS}}^2}{\left[C_1{}' Z_A \left(R_L + R_{LC}\right)\right]^2 \text{Re}\left[Z_{\text{in}}\right]}. \tag{32}$$

Based on the above analysis, the SR coil IPT system with LCC-S compensation characteristics causes no damage to the front-end power source during no-load operation and outputs approximately constant voltage as the traditional LCC-S IPT system. However, according to (16), the resonant frequency is related to the coupling coefficients, therefore, the condition for the independence of the resonant frequency from the coupling coefficients is analyzed in the following section.

IV. DIMENSION DESIGN OF COILS FOR THE LCC-S SR COIL IPT SYSTEM

This section gives the dimension design of coils for the LCC-S SR coil IPT system. First, in order to light a LED monitor with an ac load of 15 Ω at a working frequency of 13.56 MHz and a transmission distance of 35 mm, the specific equivalent circuit parameters of the LCC-S SR coil IPT system are designed according to the equivalent circuit in the previous section. Next, based on equivalent circuit parameters and the structure of the LCC SR coil and the series SR coil, an analysis of the loss mechanisms and Q(quality factor) optimization are conducted, leading to the determination of coil dimensional parameters. Finally, the independence of the resonant frequency from the coupling coefficients is analysed using this specific coil design. The parameters of the SR coil IPT system with LCC-S compensation characteristics are designed, operating at 13.56 MHz. To illuminate a LED monitor with an ac load of 15 Ω over a transmission distance of 35 mm, at least 10 W of ac output power is required. The set parameters is shown in Table I.

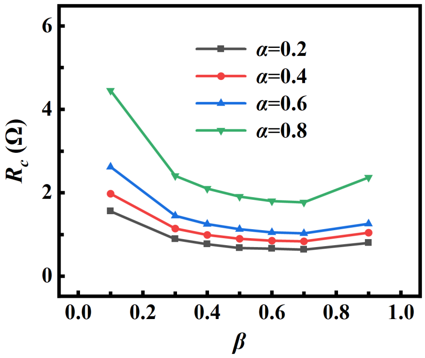

Fig. 8. Influence of β on coil loss.

A. Loss Mechanisms and Improvement of Q

To improve the performance of the proposed IPT system, Q of the three parts(*LA*, *LB*,*CA*) in primary LCC SR coil and secondary series SR coil *LC* should be optimized. Since the Q of both capacitors and inductors is inversely proportional to loss, the losses of each part must be optimized. The losses of the primary LCC SR coil are R_{LA}, R_{LB}, R_{CA}, and similarly, the loss of the secondary series SR coil is R_{LC}, as showed in the Fig. 6. The metal vias and traces used to connect the three components of the LCC SR coil exhibit negligible loss compared to R_{LA}, R_{LB}, and R_{CA}, thus only these four losses are considered. Since the loss consists of conductive loss(R_c) and dielectric loss(R_d), optimization will be pursued in both aspects.

To decrease R_c of R_{LA}, R_{LB}, and R_{LC}, the thickness of metal conductors is set to 0.07 mm, considering skin effect losses and fabrication challenges for high-frequency circuits [39]. As shown in Fig. 8, It can be seen that the optimal value of β(the ratio of the winding width w to the spacing between adjacent windings s) occurs in the range of 0.5 to 0.7, and R_c varies gradually around the optimal value of β. Thus, β is set to 0.5 for *LA*, 0.51 for *LB* and 0.7 for *LC*.

The reason why *CA* is designed as two symmetrically distributed gear-shaped metal plates on the upper and lower surfaces of the dielectric substrate is to minimize the *Rc* of *CA*. The use of gear-shaped capacitors can effectively reduce eddy currents by comparing the current distribution on the capacitor when using LCC SR coils with the gear-shaped capacitor and the traditional disc-shaped capacitor. Fig. 9 shows the LCC SR coils with the traditional disc-shaped capacitor and the gear-shaped capacitor. Both two capacitor shapes consist of two symmetrically distributed metal plates on the upper and lower surfaces of the dielectric substrate. Fig. 10 is the current distribution of the two capacitor shapes. The disk-shaped capacitor can generate eddy currents, thereby causing additional eddy current losses, as shown in Fig. 10(a) and (b). By contrast, the gear-shaped capacitor effectively suppresses eddy currents, as shown in Fig. 10(c) and (d). Therefore, the parallel capacitor of the LCC SR coil is designed as two symmetrically distributed gear-shaped metal plates on the upper and lower surfaces of the dielectric substrate.

To reduce R_d, F4BM300 was chosen as the substrate for both the primary LCC SR coil and the secondary series SR coil, owing to its dielectric constant($\varepsilon_{\text{r}} = 3.0$), low dissipation

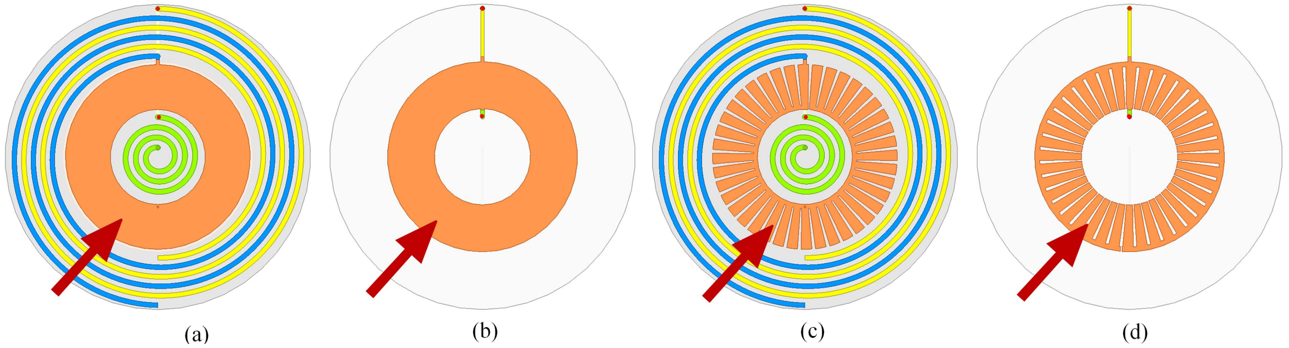

Fig. 9. LCC SR coils with the two capacitor shapes. (a) Top view of the LCC SR coil with disc-shaped capacitor. (b) Bottom view of the LCC SR coil with disc-shaped capacitor. (c) Top view of the LCC SR coil with gear-shaped capacitor. (d) Bottom view of the LCC SR coil with gear-shaped capacitor.

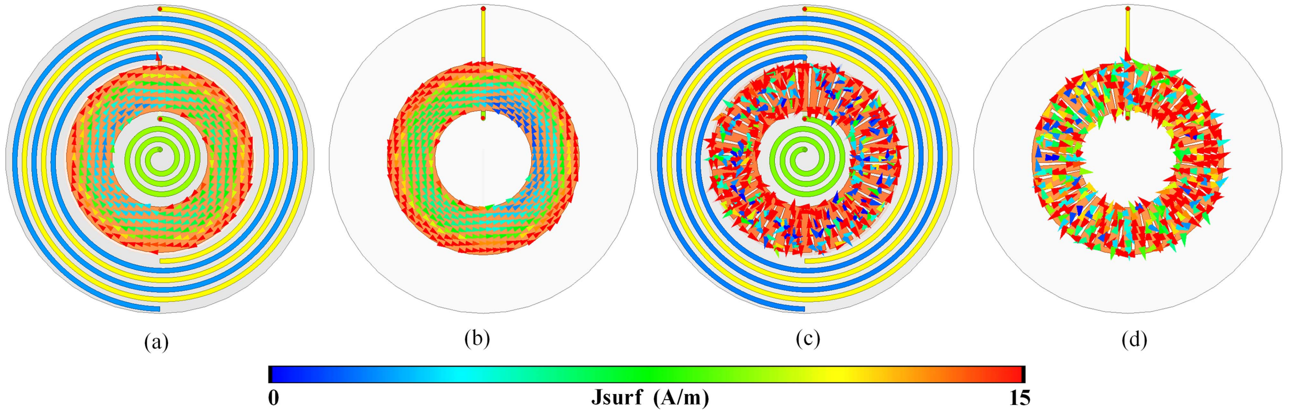

Fig. 10. Current distribution on the two capacitors when using LCC SR coils with two capacitors. (a) Top view of the LCC SR coil with disc-shaped capacitor. (b) Bottom view of the LCC SR coil with disc-shaped capacitor. (c) Top view of the LCC SR coil with gear-shaped capacitor. (d) Bottom view of the LCC SR coil with gear-shaped capacitor.

TABLE II
OPTIMIZED Q AND ASSOCIATED LOSSES OF LCC-S SR COIL IPT SYSTEM

Structural components	**Loss**	***Q***
LCC SR main coil *LA*	1.54 Ω	246.25
Compensation coil *LB*	0.53 Ω	167.2
Parallel capacitor *CA*	0.16 Ω	656.12
Series SR coil *LC*	0.85 Ω	252.1

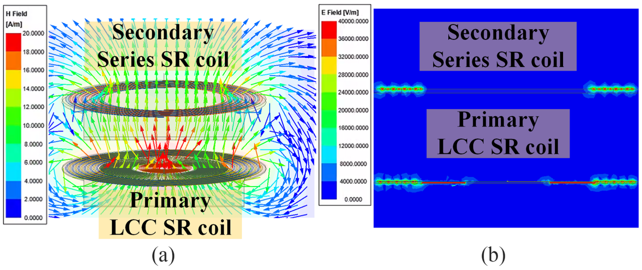

Fig. 11. Field distribution of the coils. (a) Magnetic field distribution. (b) Electric field distribution.

factor ($D_d = 0.0018$), and advantages in cost and processing complexity.

The optimized *Q* and associated losses of the structural components and the coil dimensional parameters are shown in Tables II and III. Additionly, the thicknesses of substrate for primary LCC SR coil and secondary series SR coil are 0.508 mm and 1.575 mm, respectively. The outer diameters the primary and secondary main coils are set to 100 mm to ensure a reasonable size and performance.

The magnetic field distribution of the primary and secondary coils is simulated in HFSS, as shown in Fig. 11(a). The primary LCC SR coil and the secondary series SR coil are positioned on the upper and lower sides, with the magnetic field concentrated in the region between them, forming magnetic coupling. The electric field distribution on the YOZ plane is illustrated in Fig. 11(b), where the electric field is confined around the primary and secondary coils without radiating outwards, indicating that the proposed system does not rely on the electric field for power transmission.

B. Condition for the Independence of Resonant Frequency From Coupling Coefficients

According to (16), the resonant frequency is independent of the ac load. However, apart from inductances and capacitances,

TABLE III
DIMENSIONAL PARAMETERS OF COILS

Dimensional Parameter	**Description**	**Value**
dLA_{in}	Iner diameter of *LA*	65 mm
dLA_{out}	Outer diameter of *LA*	100 mm
N_{LA}	Turn numbers of *LA*	5.5
wLA	Winding width of *LA*	0.71 mm
sLA	Winding space of *LA*	1.52 mm
dCA_{in}	Iner diameter of *CA*	32 mm
dCA_{out}	Outer diameter of *CA*	64.9 mm
w_{CA1}	Iner width of of each tooth of *CA*	0.86 mm
w_{CA2}	Outer width of of each tooth of *CA*	1.66 mm
N_{CA}	Number of teeth of *CA*	80
dLB_{in}	Iner diameter of *LB*	7.04 mm
dLB_{out}	Outer diameter of *LB*	28 mm
N_{LB}	Turn numbers of *LB*	8
dLC_{in}	Iner diameter of *LC*	49.6 mm
dLC_{out}	Outer diameter of *LC*	100 mm
N_{LC}	Turn numbers of *LC*	4.5
wLC	Winding width of *LC*	1.47 mm
sLC	Winding space of *LC*	2.1 mm

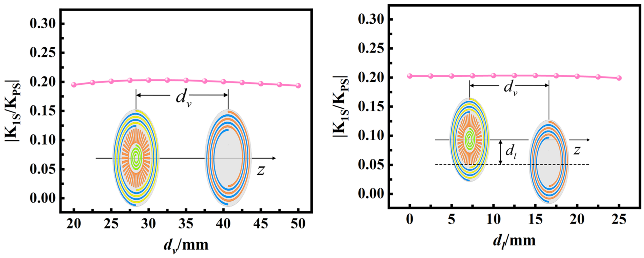

(a) (b)

Fig. 12. Variation curve of K_{1S}/K_{PS}. (a) d_v changes. (b) d_l changes at a fixed d_v of 35 mm.

the resonant frequency is also influenced by the cross-coupling coefficient K_{1P} and the ratio of coupling coefficients K_{1S}/K_{PS}. To the LCC SR coil, the compensation coil and main coil are integrated into a single unit with a fixed relative position, resulting in a constant value of K_{1P}. To determine if the resonant frequency is independent of the load and coupling coefficient during transmission, it is necessary to study the conditions under which K_{1S}/K_{PS} remains approximately constant when the coil experience vertical and lateral displacement. Since the coupling coefficient is only dependent on the coil size [22], the filament method [35], [36], [37] can be used to calculate the coupling coefficient.

Using the coil dimensions mentioned above, the ratio of the coupling coefficients K_{1S}/K_{PS} versus axial and lateral misalignment is calculated, as depicted in Fig. 12, respectively. When the axial distance (d_v) varies while the lateral misalignment distance (d_l) remains fixed at 0 mm and d_l changes while d_v remains fixed at 35 mm, the variation in K_{1S}/K_{PS} is remaining approximately constant. Therefore, under the coil dimension parameters in Table III, the resonant frequency is approximately independent of coupling coefficients, thus exhibiting good misalignment tolerance.

Next, based on the above coil dimensions, the influence of each dimensional parameter on K_{1S}/K_{PS} when d_v and d_l change is studied using the control variable method, thereby obtaining the condition for the independence of resonant frequency form the coupling coefficients. To simplify the analysis, the outer diameter of the primary main coil *LA* and secondary coil *LC* is kept constant. The dimensional parameters of each coil can be defined as

$$p = \frac{dLB_{\text{out}}}{dLA_{\text{out}}}, q = \frac{dLA_{\text{in}}}{dLA_{\text{out}}}, m = \frac{dLB_{\text{in}}}{dLB_{\text{out}}}, n = \frac{dLC_{\text{in}}}{dLA_{\text{out}}}. \quad (33)$$

Due to the requirement that the outer diameter of every coil be larger than the inner diameter, and the need to leave space for the compensation capacitor between the main coil and the compensation coil of the LCC SR coil, the parameters in (33) are defined within the following limits:

$$0.1 \leq p \leq 0.5, 0.3 \leq q \leq 0.9, 0.2 \leq m \leq 0.8, 0.2 \leq n \leq 0.8.$$

The variation curve of K_{1S}/K_{PS} when d_v changes at a fixed d_v of 0 mm and when d_l changes at a fixed d_v of 35 mm is shown in the Figs. 13 and 14. When q, m and p change, K_{1S}/K_{PS} shows small fluctuation under variations in d_v and d_l, remaining approximately constant. The primary factors influencing the fluctuation in K_{1S}/K_{PS} is n. As shown in Figs. 13(d) and 14(d), when $n = 0.6$, the fluctuation in K_{1S}/K_{PS} is smallest. Therefore, n should be designed to be 0.6. Therefore, when the outer diameters of the primary main coil *LA* and secondary coil *LC* are the same, the design of the LCC SR coil only needs to consider reserving space for the parallel capacitor *CA* and compensation coil *LB*. The key point is that the inner diameter of the secondary main coil *LC* needs to be 0.6 times its outer diameter.

V. EXPERIMENTAL VALIDATION

In this section, first, through the ac–ac experiment, the independence of the resonant frequency from the coupling coefficients obtained through theoretical calculations in Section IV and the approximately constant voltage output independent of ac Load derived from the theoretical formula in Section III, were validated through ac–ac experiment. Additionally, the transmission characteristic of high-efficiency transmission across a wide range of ac load variations is also obtained. Afterwards, a dc–dc experiment was conducted using a power analyzer, achieving a dc–dc efficiency of 80.5%. Finally, a dc–dc experiment was set up with an LED monitor serving as the load, which verifies its practical application in electronic devices.

A. Experiment of AC Transmission Characteristics

The actual coils fabricated according to the dimensions specified in Section IV are shown in Fig. 15. The ac–ac system experiment was conducted using an oscilloscope (KEYSIGHT DSOX3024T) and an ac power source to verify the approximate

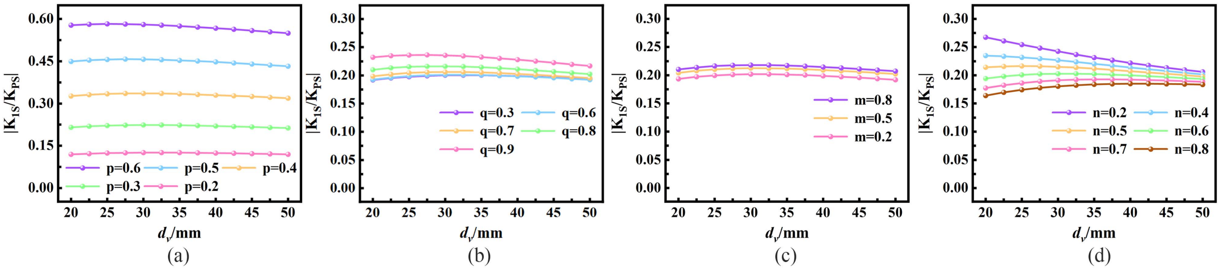

Fig. 13. Variation curve of K_{1S}/K_{PS} with changes in d_v when (a) dLB_{out} changes; (b) dLA_{in} changes; (c) dLB_{in} changes; (d) dLC_{in} changes.

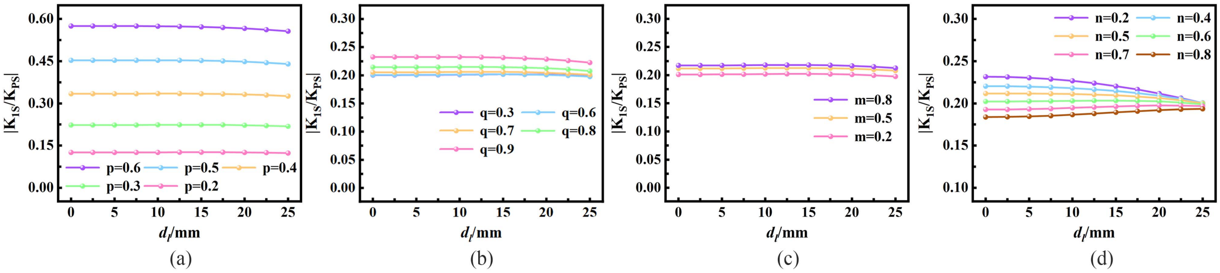

Fig. 14. Variation curve of K_{1S}/K_{PS} with changes in d_l at a fixed d_v of 35 mm when (a) dLB_{out} changes; (b) dLA_{in} changes; (c) dLB_{in} changes; (d) dLC_{in} changes.

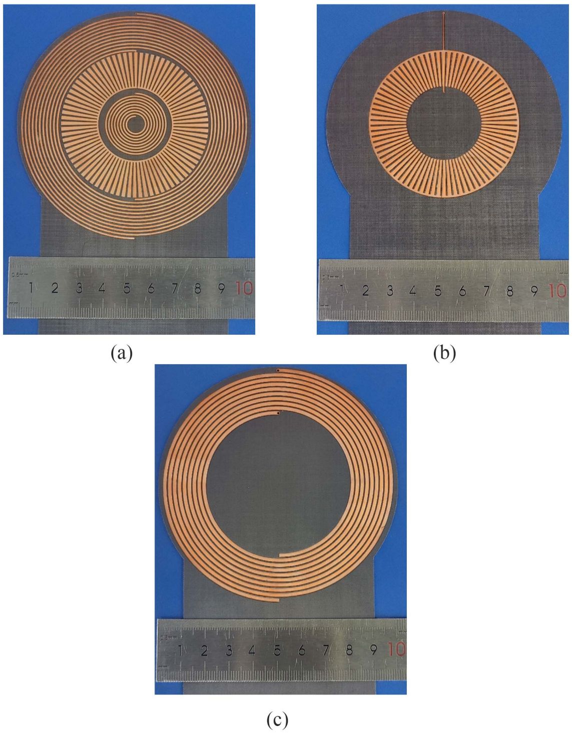

Fig. 15. Fabricated coils. (a) Top view of the LCC SR coil. (b) Bottom view of the LCC SR coil. (c) Series SR coil.

constant voltage output that is independent of the ac load discussed in Section III, as well as the independence of the resonant frequency from the coupling coefficient detailed in Section IV.

To obtain accurate waveforms at the operating frequency of 13.56 MHz, we calibrated the voltage and current probes of the oscilloscope by combining a standard ac resistor with a deskew fixture(KEYSIGHT U1880A), ensuring that the displayed voltage and current values were free of phase shift and matched the actual values of the standard resistors, thereby guaranteeing the precision of the waveforms measured by the oscilloscope. The ac–ac experimental setup was composed of an ac power source(QX-ASA100M), coupling coils and an ac load, as shown in Fig. 16(a). The power source input 13 W of ac power to the primary LCC SR coil, which was then delivered to the ac load by the secondary series SR coil. The oscilloscope was utilized to acquire and measure the input and output voltages and currents, thereby obtaining the ac–ac efficiency(η_{ac}) is obtained by dividing the output power by the input power. The power can be calculated using the following formula:

$$\bar{P} = \frac{1}{T}\int_0^T P(t)dt \tag{34}$$

where

$$P(t) = u(t) \cdot i(t) = U_0 I_0 \cos(\omega t + \varphi) \cos(\omega t)$$

where $u(t)$ and $i(t)$ are voltage and currents containing phase shift. When $R_L = 30\ \Omega$, the input and output voltage and current of the coupling coils is shown in Fig. 16(b), with the original graph directly exported from the oscilloscope.

With the ac load fixed at 15 Ω, the variation curve of input voltage-current phase difference ($\Delta\theta$) when vertical distance (d_v) between the coils was varied while maintaining zero lateral misalignment distance (d_l) is shown in Fig. 17, and the variation curve of $\Delta\theta$ when d_l was varied while keeping a fixed dv at 35 mm is shown in Fig. 18. The phase difference remains nearly constant, indicating that the resonant frequency of the

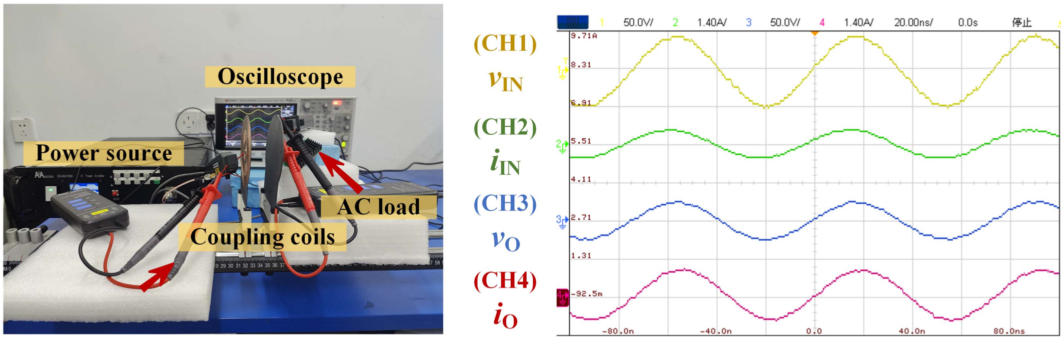

(a) (b)

Fig. 16. (a) AC–AC experimental setup of the SR coil IPT system with LCC-S compensation characteristics. (b) Measured waveforms on the oscilloscope of the proposed IPT system with an AC load of 30 Ω.

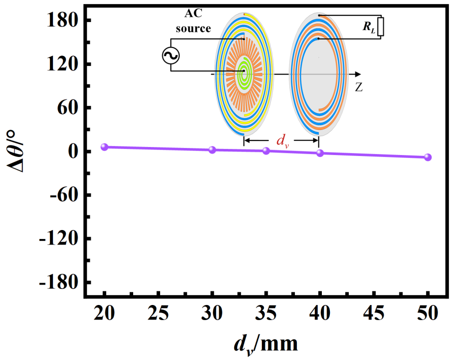

Fig. 17. $\Delta\theta$ with changes in d_v at a fixed d_l of 0 mm.

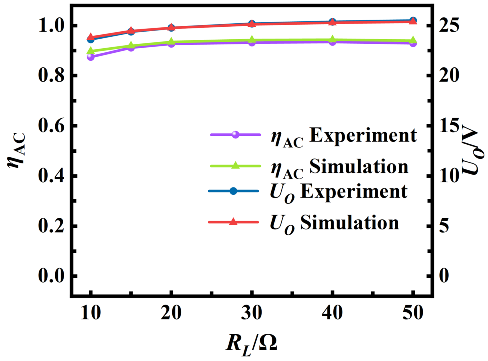

Fig. 19. η_{ac} and U_O with respect to the different R_L.

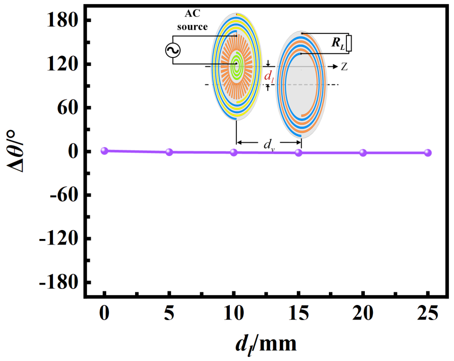

Fig. 18. $\Delta\theta$ with changes in d_l at a fixed d_v of 35 mm.

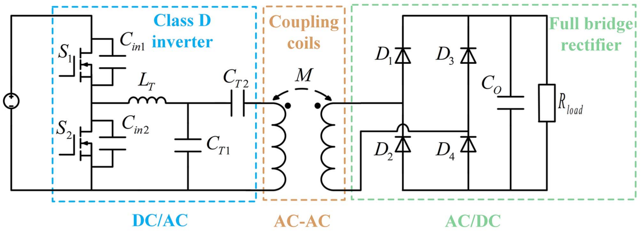

Fig. 20. DC–DC Experimental block diagram of the SR coil IPT system with LCC-S compensation characteristics.

SR coil IPT system with LCC-S compensation characteristics is independent of the coupling coefficient.

With dv between the coils fixed at 35 mm and a fixed d_l at 0, the output voltage Uo was measured across ac loads ranging from 10 Ω–50 Ω with the same input voltage of 45 V. Meanwhile, the ac transmission efficiency(η_{ac}) was measured for 10 Ω–50 Ω ac loads with the same input power of 11 W. The resulting η_{ac} curve and Uo curve are shown in Fig. 19. When R_L varies from 10 Ω to 50 Ω, the output voltage remains approximately constant, closely matching the theoretical transmission characteristics. Additionally, η_{ac} is consistently above 87%, and reaches 91.5% at 15 Ω, and the maximum η_{ac} is 93.2% at 30 Ω, demonstrating the high transmission efficiency of the SR coil IPT system with LCC-S compensation characteristics.

B. DC–DC Experiment

Based on Section V-A, with an ac load of 30 Ω yielding the maximum η_{ac} of 93.2%, an optimal dc–dc system was designed accordingly. The dc–dc system comprises a Class D zero voltage switching (ZVS) inverter [38] for dc–ac conversion, coupling coils for ac–ac transmission, and a full bridge rectifier for ac–dc conversion, with the experimental block diagram illustrated in Fig. 20. Notably, the Class D inverter consists of an inverter

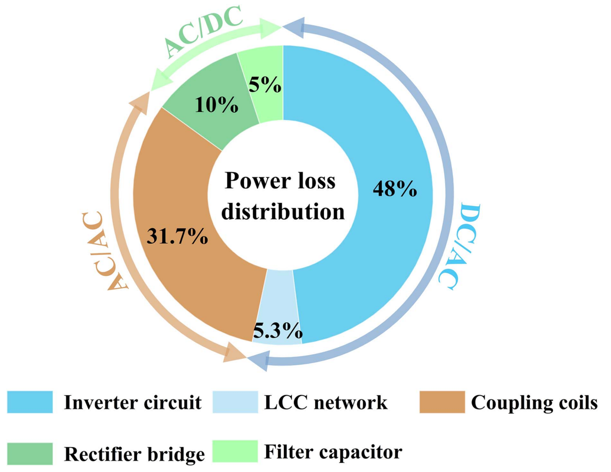

Fig. 21. Power distribution of the proposed DC–DC system.

circuit and an LCC network(L_T, C_{T1}, and C_{T2}), with the LCC network enabling both ZVS and impedance matching. The full bridge rectifier is composed of a rectifier bridge and a filter capacitor. GaN HEMT GS61008T is used as the switching components of the inverter. The component specification of the four rectifying diodes is DFLS240L Schottky diode. The power loss(P_L) distribution of the dc–dc system, simulated using Cadence PSpice is shown in the Fig. 21. The input and output power of the IPT system are 15. 68 W and 12.7 W, respectively, yielding a total P_L of 2.98 W. The main loss of the Class D inverter(dc–ac) arises from the switching losses of the two MOSFETS in the inverter circuit and the full bridge rectifier(ac–dc) is primarily due to the parasitic losses of the diodes and loss of the filter capacitor.

The dc–dc experimental setup was constructed according to the dc–dc experimental block diagram, as shown in Fig. 22(a). The dc–dc experiment was conducted using a high-precision power analyzer (ZLG PA8000P). The dc–dc efficiency (η_{dc}) was measured by connecting the voltage input terminals in parallel to both the inverter input port and rectifier output port, while simultaneously connecting the current input terminals in series to both ports. This configuration enabled precise measurement of input and output power using the power analyzer, yielding η_{dc} of 80.5% through comparative power calculations. The waveform diagram is presented in Fig. 22(b), in which the yellow and green traces represent the voltage and current waveforms at the input end of the primary LCC SR coil, respectively, while the blue and red traces represent the voltage and current waveforms at the output end of the secondary series SR coil, respectively. The dc–dc experimental setup with an LED monitor as the dc load, as shown in Fig. 23, successfully illuminated the LED monitor, demonstrating the feasibility of the IPT system.

C. Comparison

Table IV compares the LCC SR coil proposed in this article with the popular SR coils in recent years. Among them, the SR coils referenced in [12], [31], [13], and [17] feature SS and PP compensation network characteristics and exhibit high efficiency, but fail to balance safety and stability. Wang et al. [25] proposed adding lumped inductors to the existing parallel SR coils to form a high-order LCL–LCL compensation network. While this approach avoids the issue of reducing system stability caused by adding lumped capacitors, the lumped inductors result in large space requirements, a complex structure, and low transmission efficiency. The proposed LCC SR coil retains the advantages of the SR coil and LCC compensation network in enhancing integration and stability, while overcoming the

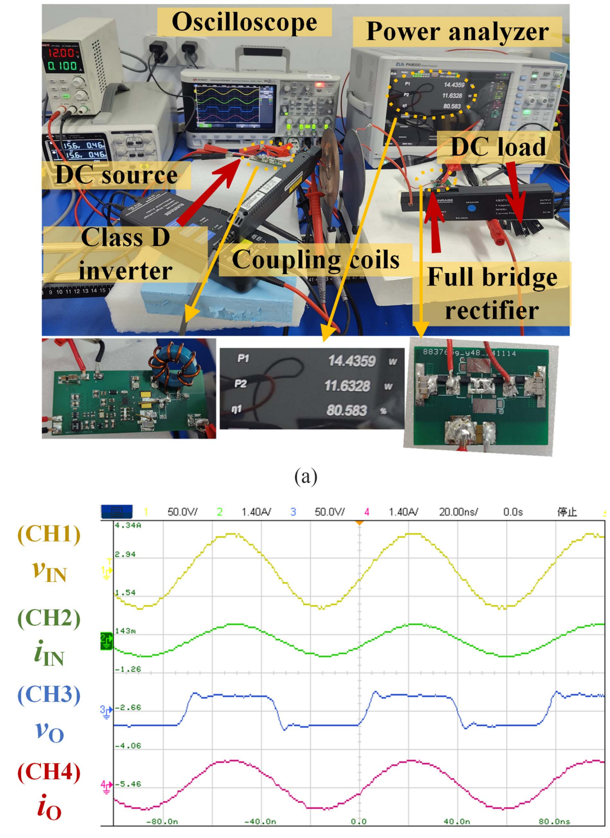

(a)

(b)

Fig. 22. (a) DC–DC Experimental setup of the SR coil IPT system with LCC-S compensation characteristics. (b) Measured waveforms on the oscilloscope of the DC–DC experiment.

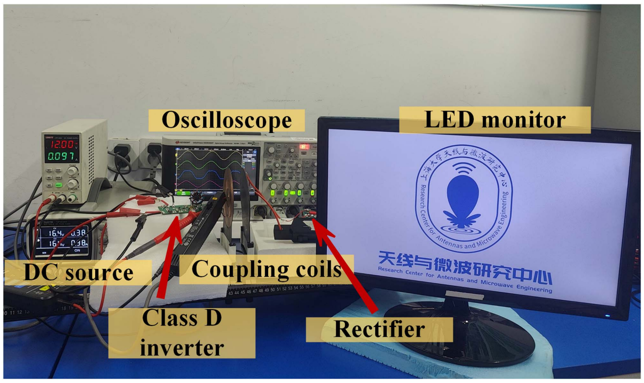

Fig. 23. LED monitor wirelessly powered by the SR coil IPT system with LCC-S compensation characteristics.

TABLE IV
COMPARISON OF REPORTED SR COILS IPT SYSTEM AND PROPOSED LCC-S SR COIL IPT SYSTEM

Ref	f (MHz)	Diameter (mm)	Height (mm)	Compensation network	η
[12]	13.56	100	2.37	SS	89.3% (ac) *NA* (dc)
[34]	13.56	274	69	SS	90% (ac) 75% (dc)
[13]	2.439	457.2	11.4(TX) 7.4(RX)	SS	*NA* (ac) 92.3% (dc)
[17]	6.78	66	16	PP	*NA* (ac) 94.6% (dc)
[25]	0.12	230	96	LCL-LCL	*NA* (ac) 67% (dc)
This work	13.56	100	0.578(TX) 1.645(RX)	LCC-S	93.2% (ac) 80.5% (dc)

shortcoming of current low-order series and parallel SR coils that cannot simultaneously achieve high safety and high stability, thus offering high integration, high stability, and high safety.

VI. CONCLUSION

In this article, a novel SR coil with LCC compensation characteristics that integrates the required compensation components in the form of distributed parameter with the main coil on a single dielectric substrate is proposed. This coil retains the advantages of the SR coils in enhancing compactness and stability, while overcoming the shortcoming of current low-order series and parallel SR coils that cannot simultaneously achieve high safety and high stability, thus offering high integration, high stability, and high safety. Through theoretical derivation and experiments, the transmission characteristics of the SR coil IPT system with LCC-S compensation characteristics was validated, confirming its a constant voltage output independent of the ac load, high η_{ac} over a wide range of ac load values, independence of resonant frequency from coupling coefficients, and no damage to the front-end power source during no-load operation. Experimental results demonstrate an η_{ac} of 93.2% over a 35 mm spacing gap. In addition, η_{dc} can reach 80.5%, and a LED monitor is successfully powered, indicating its potential for application in electronic devices, such as mobile phones and laptops.

REFERENCES

[1] A. Mahesh, B. Chokkalingam, and L. Mihet-Popa, “Inductive wireless power transfer charging for electric vehicles—A review,” *IEEE Access*, vol. 9, pp. 137667–137713, 2021.

[2] G. A. Covic and J. T. Boys, “Inductive power transfer,” *Proc. IEEE*, vol. 101, no. 6, pp. 1276–1289, Jun. 2013.

[3] Y. Wang, Z. Sun, Y. Guan, and D. Xu, “Overview of megahertz wireless power transfer,” *Proc. IEEE*, vol. 111, no. 5, pp. 528–554, May 2023.

[4] V. Ramakrishnan et al., “A comprehensive review on efficiency enhancement of wireless charging system for the electric vehicles applications,” *IEEE Access*, vol. 12, pp. 46967–46994, 2024.

[5] H.-J. Kim, H. Hirayama, S. Kim, K. J. Han, R. Zhang, and J.-W. Choi, “Review of near-field wireless power and communication for biomedical applications,” *IEEE Access*, vol. 5, pp. 21264–21285, 2017.

[6] A. Kuperman, “Additional two-capacitor basic compensation topologies for resonant inductive WPT links,” *IEEE Trans. Power Del.*, vol. 35, no. 5, pp. 2568–2570, Oct. 2020.

[7] W. Li, H. Zhao, J. Deng, S. Li, and C. C. Mi, “Comparison study on SS and double-sided LCC compensation topologies for EV/PHEV wireless chargers,” *IEEE Trans. Veh. Technol.*, vol. 65, no. 6, pp. 4429–4439, Jun. 2016.

[8] C. M. de Miranda and S. F. Pichorim, “A self-resonant two-coil wireless power transfer system using open bifilar coils,” *IEEE Trans. Circuits Syst. II, Exp. Briefs.*, vol. 64, no. 6, pp. 615–619, Jun. 2017.

[9] R. Narayanamoorthi and A. V. Juliet, “Capacitor-less high-strength resonant wireless power transfer using open bifilar spiral coil,” *IEEE Trans. Appl. Supercond.*, vol. 29, no. 1, Jan. 2019, Art. no. 5500108.

[10] C. M. de Miranda and S. F. Pichorim, “Alternative configuration of openbifilar coil for self-resonant wireless power transfer system,” in *Proc. IEEE Wireless Power Transfer Conf.*, 2019, pp. 116–119.

[11] N. Haga, J. Chakarothai, and K. Konno, “Circuit modeling of a wireless power transfer system containing ferrite shields using an extended impedance expansion method,” *IEEE Trans. Microw. Theory Techn.*, vol. 70, no. 5, pp. 2872–2881, May 2022.

[12] Z. Yi, M. Li, B. Muneer, G. He, and X.-X. Yang, “Self-resonant antisymmetric planar coil for compact inductive power transfer system avoiding compensation circuits,” *IEEE Trans. Power Electron.*, vol. 36, no. 5, pp. 5121–5134, May 2021.

[13] R. Qin, J. Li, J. Sun, and D. Costinett, “Shielding design for high-frequency wireless power transfer system for EV charging with self-resonant coils,” *IEEE Trans. Power Electron.*, vol. 38, no. 6, pp. 7900–7909, Jun. 2023.

[14] J. Xiang, C. Q. Jiang, T. Ma, Y. Wang, and Y. Fan, “An ultra-thin selfresonant coupler with nanocrystalline flake ribbons for wireless power transfer system,” *IEEE Trans. Magn.*, vol. 60, no. 9, Sep. 2024, Art. no. 8600805.

[15] J. Xiang, C. Q. Jiang, T. Ma, X. Wang, Y. Fan, and J. Zhou, “High power density self-resonant coupler for flexible surface wireless power transfer system with nanocrystalline ribbon,” *IEEE Trans. Power Electron.*, vol. 39, no. 10, pp. 13975–13987, Oct. 2024.

[16] R. Qin, J. Li, and D. Costinett, “A 6.6-kW high-frequency wireless power transfer system for electric vehicle charging using multilayer nonuniform self-resonant coil at MHz,” *IEEE Trans. Power Electron.*, vol. 37, no. 4, pp. 4842–4856, Apr. 2022.

[17] L. Gu, G. Zulauf, A. Stein, P. A. Kyaw, T. Chen, and J. M. R. Davila, “6.78-MHz wireless power transfer with self-resonant coils at 95% DC–DC efficiency,” *IEEE Trans. Power Electron.*, vol. 36, no. 3, pp. 2456–2460, Mar. 2021.

[18] Z. Yi, K. Yang, X.-X. Yang, M. Li, and D. Zeng, “A gradual-width high- Q self-resonant coil based on coplanar waveguide,” *IEEE Microw. Wireless Technol. Lett.*, vol. 35, no. 2, pp. 165–168, Feb. 2025, doi: 10.1109/LMWT.2024.3506987.

[19] L. Zhu, L. Wang, C. Zhao, J. Shen, M. Wu, and L. Pei, “Design and optimization of unequal-pitch self-resonant helical coils for high-efficiency mid-range wireless power transfer,” *IEEE Trans. Power Electron.*, vol. 39, no. 11, pp. 15281–15294, Nov. 2024.

[20] L. Zhu, L. Wang, M. Wu, C. Zhao, and L. Yu, “Precise modeling and design of self-resonant for high-efficiency mid-range wireless power transfer system,” *IEEE Trans. Power Electron.*, vol. 38, no. 6, pp. 7848–7862, Jun. 2023.

[21] M. Kim and J. Choi, “Design of self-resonant spiral coils for mid-range, high-frequency wireless power transfer systems,” in *Proc. Wireless Power Week*, 2022, pp. 33–38.

[22] F. Lu, H. Zhang, H. Hofmann, W. Su, and C. C. Mi, “A dual-coupled LCC-compensated IPT system with a compact magnetic coupler,” *IEEE Trans. Power Electron.*, vol. 33, no. 7, pp. 6391–6402, Jul. 2018.

[23] H. Wang, J. Sun, and K. W. E. Cheng, “A compact and integrated magnetic coupler design with cross-coupling elimination utilizing LCC-S compensation network for building attached photovoltaic systems,” *IEEE Trans. Magn.*, vol. 59, no. 11, Nov. 2023, Art. no. 8401205.

[24] V. Shevchenko, O. Husev, R. Strzelecki, B. Pakhaliuk, N. Poliakov, and N. Strzelecka, “Compensation topologies in IPT systems: Standards, requirements, classification, analysis, comparison and application,” *IEEE Access*, vol. 7, pp. 120559–120580, 2019.

[25] Q. Wang, M. A. Saket, A. Troy, and M. Ordonez, “A self-compensated planar coil for resonant wireless power transfer systems,” *IEEE Trans. Power Electron.*, vol. 36, no. 1, pp. 674–682, Jan. 2021.

[26] X. Wang, J. Xu, M. Leng, H. Ma, and S. He, “A hybrid control strategy of LCC-S compensated WPT system for wide output voltage and ZVS range with minimized reactive current,” *IEEE Trans. Ind. Electron.*, vol. 68, no. 9, pp. 7908–7920, Sep. 2021.

[27] Q. Wang et al., “Inductive power transfer system with constant current-constant voltage charging tolerating misalignment based on multi-objective optimization for compensation topology,” *IEEE Trans. Power Electron.*, vol. 40, no. 3, pp. 4581–4591, Mar. 2025.

[28] S. Li, F. Li, R. Zhang, C. Tao, and L. Wang, “Accurate modeling, design and load estimation of LCC-S based WPT system with a wide range of load,” *IEEE Trans. Power Electron.*, vol. 38, no. 10, pp. 11763–11775, Oct. 2023.

[29] S. Li, W. Li, J. Deng, T. D. Nguyen, and C. C. Mi, “A double-sided LCC compensation network and its tuning method for wireless power transfer,” *IEEE Trans. Veh. Technol.*, vol. 64, no. 6, pp. 2261–2273, Jun. 2015.

[30] X. Wang, R. He, H. Wang, J. Liang, and M. Fu, “Modified LCC compensation and magnetic integration for inductive power transfer,” *IEEE J. Emerg. Sel. Topics Power Electron.*, vol. 12, no. 1, pp. 186–194, Feb. 2024.

[31] Y. Wang, F. Wang, Y. Tian, A. Sun, and B. Liu, “Surrogate-assisted multiobjective optimization of double-D coil for inductive power transfer system with LCC–LCC compensation network,” *IEEE Trans. Ind. Electron.*, vol. 71, no. 9, pp. 10612–10624, Sep. 2024.

[32] C. M. de Miranda and S. F. Pichorim, “Alternative configuration of openbifilar coil for self resonant wireless power transfer system,” in *Proc. IEEE Wireless Power Transfer Conf.*, 2019, pp. 116–119.

[33] Z. Yi, A. Liu, B. Zhou, X.-X. Yang, and M. Li, “A novel interdigital self-resonant coil for inductive power transfer,” *IEEE Microw. Wireless Technol. Lett.*, vol. 33, no. 9, pp. 1369–1372, Sep. 2023.

[34] Z. Yi, M. Li, B. Muneer, and Q. Zhu, “High-efficiency mid-range inductive power transfer employing alternative-winding coils,” *IEEE Trans. Power Electron.*, vol. 34, no. 7, pp. 6706–6721, Jul. 2019.

[35] S. Westerlund and L. Ekstam, “Capacitor theory,” *IEEE Trans. Dielectrics Elect. Insul.*, vol. 1, no. 5, pp. 826–839, Oct. 1994.

[36] S. I. Babic and C. Akyel, “New analytic-numerical solutions for the mutual inductance of two coaxial circular coils with rectangular cross section in air,” *IEEE Trans. Magn.*, vol. 42, no. 6, pp. 1661–1669, Jun. 2006.

[37] C. Akyel, S. I. Babic, and M. M. Mahmoudi, “Mutual inductance calculation for non-coaxial circular air coils with parallel axes,” *Prog. Electromagn. Res.*, vol. 91, pp. 287–301, 2009.

[38] S. Babic, F. Sirois, C. Akyel, and C. Girardi, “Mutual inductance calculation between circular filaments arbitrarily positioned in space: Alternative to Grover’s formula,” *IEEE Trans. Magn.*, vol. 46, no. 9, pp. 3591–3600, Sep. 2010.

[39] S. Li, Y. Xiao, R. Ma, M. Liu, and C. Ma, “LCC matching network design for a MHz class D GaN PA considering parameter uncertainties,” in *Proc. IEEE Wireless Power Technol. Conf. Expo*, 2024, pp. 682–687.

[40] A. Liu, “Research on ultra-thin high-Q self-resonant coils for wireless power transfer,” M.S. thesis, Dept. Commun. and Info. Eng., Shanghai Univ., Shanghai, China, 2023.

Zixuan Yi (Member, IEEE) was born in Taiyuan, China, in 1991. He received the B.S. degree in electronic engineering and information science from the University of Science and Technology of China, Hefei, China, in 2014, and the Ph.D. degree in electromagnetism field and microwave technology from the University of Science and Technology of China, Hefei, China, in 2016.

He is currently a Lecturer with the School of Communication and Information Engineering, Shanghai University. His research interests include wireless power transfer systems, microwave passive components, microwave integrated circuits, and antennas.

Qingfei Zhang (Student Member, IEEE) was born in Shanghai, China, in 2000. He received the B.S. degree in communication engineering in from Jiangsu University, Zhenjiang, China, in 2022. He is currently working toward the M.E. degree in electromagnetic fields and microwave techniques with the School of Communication and Information Engineering, Shanghai University, Shanghai, China.

His research interests include wireless power transfer and high-frequency power supply.

Shuang Li (Student Member, IEEE) received the B.S. degree in Automation from Harbin Institute of Technology, Shenzhen, Shenzhen, China, in 2022, and the M.S. degree in Control Science and Engineering from Shanghai Jiao Tong University, Shanghai, China, in 2025. He is currently pursuing the Ph.D. degree in Control Science and Engineering at the University of Michigan-Shanghai Jiao Tong University Joint Institute, Shanghai Jiao Tong University, Shanghai, China.

His research interests include MHz power electronics, with a focus on MHz wireless power transfer systems.

Xue-Xia Yang (Senior Member, IEEE) received the B.S. and M.S. degrees in radio physics from Lanzhou University, Lanzhou, China, in 1991 and 1994, respectively, and the Ph.D. degree in electromagnetic field and microwave technology from Shanghai University, Shanghai, China, in 2001.

From 1994 to 1998, she was a Teaching Assistant and a Lecturer with Lanzhou University, China. From 2001 to 2008, she was a Lecture and an Associate Professor in Shanghai University, China. She is currently a Professor and the Head with the Antennas and Microwave R&D Center, Shanghai University. She has authored or coauthored more than 180 technical journal and conference papers. She is also a frequent Reviewer for more than 10 scientific journals. Her research interests include antennas theory and technology, computational electromagnetics, and microwave power transmission.

Dr. Yang is currently a Member of the Committee of Antenna Society of China Electronics Institute and Senior Member of China Electronics Institute. She is an Associate Editor for the *Journal of Shanghai University* (Science edition).

Dan Zeng (Senior Member, IEEE) received the B.S. degree in electronic science and technology and the Ph.D. degree in circuits and systems from the University of Science and Technology of China, Hefei, China. She is currently a Full Professor and the Dean with the Department of Communication Engineering, Shanghai University, directing the Computer Vision and Pattern Recognition Laboratory. Her main research interests include computer vision, multimedia analysis, wireless power transfer, and machine learning.

Dr. Zeng is a TC Member of IEEE Multimedia Systems and Applications and IEEE International Workshop on Multimedia Signal Processing. She is serving as a Vice Chair for IEEE COMSOC MMTC Exco Committee.

Meiling Li (Member, IEEE) was born in Wuhu, China, in 1988. She received the B.S. degree in electronic information engineering from Anhui University, Hefei, China, in 2010, and the Ph.D. degree in electromagnetism field and microwave technology from the University of Science and Technology of China, Hefei, China, in 2016.

She was a Postdoctoral Researcher with the Department of Electronic Engineering and Information Science, University of Science and Technology of China. She is currently a Lecturer with the School of Communication and Information Engineering, Shanghai University. Her research interests include wireless power transfer systems, frequency selected surfaces, absorbing materials and structures, and microwave circuits.